

Naval Oceanographic
and Atmospheric
Research Laboratory

Technical Note 123
August 1991

AD-A241 909



6 7 10 8
②

Sea Surface Environmental Conditions in the Gulf of Alaska During April 1990, Using SSM/I

DTIC
ELECTE
OCT 08 1991
S B D

P. M. Smith
Remote Sensing Branch
Ocean Sensing and Prediction Division
Ocean Science Directorate



Approved for public release; distribution is unlimited. Naval
Oceanographic and Atmospheric Research Laboratory, Stennis Space
Center, Mississippi 39529-5004.

91-12565



91

123

These working papers were prepared for the timely dissemination of information; this document does not represent the official position of NOARL.

ABSTRACT

The Special Sensor Microwave Imager (SSM/I) is capable of mapping sea surface roughness characteristics and sea foam coverage from space in most weather conditions. The SSM/I also measures precipitation and water vapor content of the atmosphere, providing a simultaneous weather analysis complementing the sea surface roughness measurements. This combination of measurements can provide input into numerical models of sound transmission in the ocean—particularly those incorporating forward scattering from the sea surface, absorption by bubbles, and the generation of noise by wind.

This technical note presents a demonstration of these capabilities for the month of April 1991 for the Gulf of Alaska. An algorithm is applied to several SSM/I passes to produce maps of root mean squared wave slope, percent sea foam coverage, precipitation, and water vapor. Two wind events are treated that were associated with the passage of low pressure systems into the gulf from the southwest. A method of deriving significant wave height from wave slope variance, using independent estimates of the dominant wavelength, is also presented.



ACKNOWLEDGMENTS

This work was supported by Program Element No. 63704N, LCDR W. A. Cook, Program Manager, Space and Naval Warfare Systems Command. Mr. Fred Abel, Jr. of Sverdrup Technology Inc. processed the infrared imagery.

Accession For	
NTIS GRA&I	<input checked="checked" type="checkbox"/>
DTIC TAB	<input type="checkbox"/>
Unannounced	<input type="checkbox"/>
Justification	
By	
Distribution/	
Availability Codes	
Dist	Avail and/or Special
A-1	

Sea Surface Environmental Conditions in the Gulf of Alaska During April, 1990 Using SSM/I

Introduction

The sea surface temperature (SST) climate in the Gulf of Alaska is dominated by the subarctic front, located near 42°N , and the Alaskan Coastal Current (ACC). Both of these features result from a cyclonic recirculation along the Alaskan Coast of the Oyashio Current extension. Figure 1 is a map of mean SST for April abstracted from Brower et al. (1977). The coolest water lies along the Aleutian Island Chain with the water warming gradually toward the southeast. There is no sea ice in the gulf; however, the ice pack in the Bering Sea just west of the Aleutians extends down to near 58°N . The shape of the isotherms in the gulf reflects the warming effect of the westward flowing ACC.

The weather in the gulf is dominated by low pressure systems which move into the gulf from the southwest. These systems keep the gulf cloud-covered for most of the time. Atmospheric fronts moving south across the Aleutians periodically clear out the clouds in the western Gulf allowing imaging of the SST by the National Oceanic and Atmospheric Administration (NOAA) series of weather satellites. Brower et al. (1977) report that the air column stability is equally likely to be stable or unstable over the Gulf, with a standard deviation in the distribution of air-sea temperature difference of about 3°C .

The environmental data presented here includes (1) in situ data collected from the NOAA Data Buoy #46003 located at 51.9°N , 155.9°W , (2) infrared imagery from the Advanced Very High Resolution Radiometer (AVHRR) on the polar-orbiting NOAA-10 satellite, and (3) the microwave radiometer scanner data from the Special Sensor Microwave Imager (SSM/I).

Figure 2 is an infrared image of the western Gulf collected by the NOAA-10 satellite on 10 April. The ACC can be seen flowing southwest adjacent to the Aleutian Island Chain. It appears to have been blocked by the presence of an anticyclonic eddy centered at 53°N , 158°W .

Wind speeds recorded at NOAA Data Buoy #46003 were uncharacteristically low for the month of April 1990. Brower et al. (1977) report a mean wind speed for the month of April, near the buoy, of 9 m/s . However, the buoy recorded two "wind events" during April. The first occurred on 5 April and lasted 48 hours. Recorded wind speeds were approximately 12 m/s . The second event occurred on 18 April and lasted for about 12 hours. Maximum wind speed at this time was about 11 m/s . Figure 3 shows the buoy-recorded wind speed records for these two events together with the air-sea temperature differences. The thick arrows indicate the times at which the SSM/I passed overhead. The air column was recorded as being in the stable regime for the duration of both events. Figure 4 shows the wave elevation frequency spectrum recorded by the

buoy on 5 April and 19 April, respectively. Before presenting the data from the SSM/I, I will present a brief description of this instrument.

Geophysical Information from the SSM/I

The SSM/I is a passive microwave radiometer that is mounted on the DMSP satellite. The SSM/I antenna executes a conical scan of the earth's surface at a constant incidence angle of 53.1° and collects data when the antenna is looking aft (for F8) or forward (for F10). The radiometer operates at 4 frequencies, 19 GHz, 22 GHz, 37 GHz, and 85 GHz. Only the lower 3 frequencies are used in this analysis. In addition, the 19 and 37 GHz employ two polarizations (horizontal and vertical) each. These five channels are used, in combination, to discriminate the geophysical quantities, water vapor, sea surface temperature, cloud water, root mean squared (RMS) wave slope, and percent sea foam coverage, — one from another. Each of these quantities is quadratically related to the five SSM/I channels, described above, through the functional relationship:

$$\vec{G} = \vec{G}_0 + \frac{\partial \vec{G}}{\partial \vec{T}_b} \vec{\delta} + \frac{1}{2} \frac{\partial^2 \vec{G}}{\partial \vec{T}_b^2} \vec{\delta}^2$$

where

$$\vec{G} = (WS \quad FM \quad CW \quad WV \quad SST),$$

$$\vec{T}_b = (T_{19V} \quad T_{19H} \quad T_{22V} \quad T_{37V} \quad T_{37H})$$

and

$$\vec{\delta} = \vec{T}_b - \vec{T}_0$$

where

$$\vec{T}_0 = (\bar{T}_{19V} \quad \bar{T}_{19H} \quad \bar{T}_{22V} \quad \bar{T}_{37V} \quad \bar{T}_{37H}).$$

The SSM/I senses water vapor through a combination of vapor absorptive and emissive properties—that is, the vapor absorbs radiation coming from the sea surface, but radiates energy itself. RMS wave slope is sensed by a combination of polarization mixing and reflection of warm horizon temperatures into the receiving antenna. Sea foam is sensed by its unusually “warm” signature — the emissivity of foam is close to that of a black body in contrast with the relatively cold background sea. Sea surface temperature is sensed in accordance with Stefan-Boltzmann law, which states that a warmer body emits more radiant energy than a cold body. The temperature sensitivity is rather weak at the SSM/I frequencies, however. Clouds and rain are detected due to Mie and Rayleigh scattering from water droplets and ice crystals.

I present, in this technical note, maps of percent sea foam coverage and RMS wave slope due to their relevance to the scattering and absorption of acoustic

energy at the ocean surface. Additionally, maps of water vapor are presented with regions of precipitation delineated so that the position of atmospheric fronts can be seen relative to the gradients in sea surface properties. Also, the water vapor concentration aids the interpretation of the sea foam maps since, in regions of very high vapor, sea foam retrievals become difficult. In fact, the examples included in this technical note show that the sea foam algorithm often returns negative values when the water vapor concentration exceeds 20 kg/m^2 .

The surface pressure analysis provided by the National Weather Service for the periods 5–6 April and 17–18 April are qualitatively summarized on the atmospheric frontal maps shown in figure 5. In both cases lows move into the Gulf of Alaska from the southwest. In each case a low moves over the NOAA data buoy where it becomes stationary. The trailing cold front, then, rotates cyclonically about the low, ultimately becoming a warm front.

Figures 6 and 7 show SSM/I wave slope, sea foam concentration, and water vapor/precipitation for the 5–6 April time frame. RMS wave slope is measured in units of wind speed. The reported wave slope is that value of wind speed which would exist in equilibrium with the sea under neutrally buoyant conditions. The conversion to wave slope is accomplished through the expression,

$$\sigma_s^2 = 0.003 + 0.00512W$$

(Cox and Munk, 1954).

At 0440 on 5 April a front approaches the buoy from the west and wave slopes of 10 m/s are seen south of the buoy and along the approaching cold front. Slopes at the buoy are seen to be about 8 m/s. Throughout the following 36 hours the wave slopes at the buoy location remain at about the same value; however, during the 1621 pass on 5 April, values of 12 m/s to the southwest of the buoy can be seen. The data buoy recorded wind speeds from 11 to 15 m/s during this time period—a factor of 1.5 greater than the equivalent wave slopes recorded by the SSM/I. Since the atmospheric boundary layer is shown to be stable according to the buoy temperatures, the sea state may be depressed below what it would have been under neutrally buoyant conditions. High sea foam values correlate with high wind speeds behind the front as would be expected.

Figures 8, 9, and 10 show the SSM/I data for the second wind event that occurred during the 17, 18, and 19 April time window. Reference to figure 5 shows that this event coincided with the confluence of two low-pressure systems—the first system became stationary near the data buoy on 17 April and the second low approached the first from the southwest on 18 April. Figure 8 shows a front moving cyclonically around the stationary low on 17 April. Seas are fairly mild in the vicinity of the buoy. Steeper slopes (8 m/s) appear to the south near 38°N in advance of the approach of the second low-pressure system. On 18 April this disturbed area of sea has moved north to 48°N and exhibits slopes of order 10 m/s. Slopes near the buoy still show moderate values of 3–4 m/s. On

the afternoon of 18 April sea slopes near the buoy increase to 5-6 m/s. By 0500 on 19 April the second low is approaching the buoy with the front extending NW-SE (figure 10). Note that in the area of precipitation and high water vapor the algorithm produces negative values for sea foam coverage. SSM/I wave slopes in the vicinity of the buoy are down to 4 m/s, in close agreement with the buoy-reported wind speed.

Relevance of the SSM/I Data to Acoustic Scattering from the Air-sea Interface

The model of the emissivity of a roughened sea incorporates the Kirchhoff scattering approximation whereby it is assumed that the radius of curvature of the surface is always much greater than an electromagnetic wavelength. For electromagnetic scattering at the microwave frequencies of the SSM/I, the wavelength lies between 1.8 cm and 8 mm, and the Kirchhoff assumption is almost always satisfied. Similarly, for the forward scatter of acoustic energy from the underside of the sea surface, the Kirchhoff approximation has been shown to hold for wavelengths less than the correlation length that is typically the wavelength of the dominant wave (Thorsos, 1988). Hence, for acoustic frequencies less than 1000 Hz, the Kirchhoff approximation should hold.

However, within the Kirchhoff approximation, a second approximation must be made in order to evaluate the scattering integral. For microwave scattering, the large amplitude approximation applies and results in the expression for bistatic scattering coefficient:

$$\sigma = \frac{(kq|U|)^2}{2q_z^4\sigma_s^2} \exp \left[-\frac{q_x^2 + q_y^2}{2q_z^2\sigma_s^2} \right] \quad (1)$$

where σ_s^2 is the wave slope variance, k , is the electromagnetic wavenumber, and q_x , q_y , q_z , and q are geometric factors (Ulaby et al., 1982). In this approximation, scattering is largely incoherent.

However, for acoustic scattering from the underside of the sea surface, the longer wavelengths, especially for frequencies between 30 and 1000 Hz, preclude using the large amplitude approximation. Figure 11 shows the significant wave height required at various incidence angles, for the large amplitude approximation (equation 1) to apply at different wavelengths. This approximation is applicable only above acoustic frequencies of 1000 Hz for normal sea state conditions.

Therefore, a small slope approximation is applied in the case of acoustic scattering for RMS slopes less than 0.25. The bistatic scattering expression now involves a coherent as well as a noncoherent contribution:

$$\sigma_{coh} = \pi k^2 |a_0|^2 \delta(q_x) \delta(q_y) e^{-q_z^2 \sigma_h^2} \quad (2a)$$

$$\sigma_{incoh} = (|a_0|kl/2)^2 \exp(-q_x^2 \sigma_h^2) \sum_{n=1}^{\infty} \frac{(q_x^2 \sigma_h^2)^n}{n!n} \exp\left[-\frac{(q_x^2 + q_y^2)l^2}{4n}\right] \quad (2b)$$

where l is the coherence length of the surface, σ_h^2 is the wave height variance, and δ is the Dirac delta function. Note that equations 2a and 2b, which describe acoustic scattering, use the sea surface height variance, whereas equation 1, which describes microwave scattering, uses the sea surface slope variance. Therefore, in order to make the microwave measurement relevant to the acoustic scattering problem, we must be able to derive the height variance from the slope variance. The derivation of such a relationship is described in what follows.

Obtaining Significant Wave Height from Wave Slope Variance

As shown by Ulaby et al. (1981), Appendix 12F, the surface height variance may be related to the slope variance through the normalized autocorrelation function, $\rho(\tau)$:

$$\sigma_h^2 = \frac{-\sigma_s^2}{\rho''(0)}. \quad (3)$$

Hence, if ρ were known, the microwave radiometer measurement of σ_s could be used to infer σ_h .

I propose that the wavenumber energy spectrum can be approximated as a Gaussian with zero mean—at least in the “equilibrium” range of wavenumbers. Since the second derivative of the autocorrelation function is the transform of the power spectrum weighted by k^2 , the most important contributions to ρ will come from the high wavenumber end of the spectrum. The error due to the disparity between the Gaussian and the real sea wave spectra at low wavenumbers will, therefore, be minimized. The problem then reduces to fitting the candidate spectral function,

$$P(k) = \frac{A}{\sqrt{2p}} e^{-k^2/4p} \quad (4)$$

to a canonical form of the wavenumber spectrum, the Pierson-Moskowitz (P-M) spectrum,

$$P(k) = .159k^{-3.5} \exp[-1.25(k_{max}/k)]. \quad (5)$$

Here the P-M spectrum has been converted to a wavenumber spectrum from a frequency spectrum by substituting the dispersion relation for deep-water waves. k_{max} , in equation 5 can be interpreted as the dominant wavenumber—the wavenumber corresponding to the peak in the power spectrum.

Equation 4 is then fit to the P-M spectrum for wavenumbers in the equilibrium range. Figure 12 shows the fit for a dominant wavelength of 10 m (light

wind). Fits are performed for dominant wavelengths of 100, 50, 40, 30, 20, and 10 m and the resulting fitting parameters, p , are plotted against the corresponding k_{max} in figure 13. The data fit the polynomial,

$$p = .512k_{max}^2 \quad (6)$$

quite closely.

The candidate spectral function, equation 4, corresponds to the following Gaussian normalized autocorrelation function through the Wiener-Khinchin theorem:

$$\rho(r) = e^{-pr^2}. \quad (7)$$

$\rho''(0)$, then becomes,

$$\rho''(0) = -2p$$

or

$$\rho''(0) \simeq -k_{max}^2 \quad (8)$$

after substituting from equation 6, above. Finally, equation 3 becomes

$$\sigma_h^2 = \frac{\sigma_s^2}{k_{max}^2} \quad (9)$$

after substitution from equation 8. Equation 9 quantifies the observation that, for waves of given significant wave height, the waves are steeper, the shorter the dominant wavelength. But more importantly, if we are to relate the wave slope variance provided by the SSM/I to the wave height variance desired by the acoustic scattering modelers, we must have a minimal knowledge of the wave number spectrum—the wave length of the dominant wave.

For the period of April 1990, treated here, I use the peak frequency measured at the NOAA data buoy #46003 (See figure 4) and convert it to a dominant wave number in order to translate maps of RMS wave slope into maps of significant wave height (SWH). Examples for 5 April and 18 April are shown in figures 14 and 15.

DISCUSSION

The U.S. Navy acquired a powerful tool for the analysis of the sea surface roughness characteristics with the launch of the first SSM/I in June of 1987. This microwave radiometric scanner is sensitive to both the sea surface emissive properties and the atmospheric water vapor and cloud water. Although this sensitivity to a multitude of air and sea surface characteristics complicates the parameter retrieval problems, it also affords the opportunity to observe atmospheric forcing (water vapor fronts and precipitation) functions and the sea

surface response (whitecap population and RMS wave slope) to these functions simultaneously.

This information can be particularly valuable to the estimation of acoustically relevant properties of the sea surface—ambient noise source levels, absorption by bubble clouds, and surface scattering by ocean waves.

I have presented several examples of analysis maps, derived from SSM/I data, that can be used to nowcast and hindcast the performance of acoustic systems that depend on surface reverberation, ambient noise, and surface absorption from bubble clouds. To date, the surface scattering properties of the sea surface have been parameterized by the sea surface height variance (Ex: Clay and Medwin, 1977). Since the SSM/I is not directly sensitive to the wave height variance but to the wave slope variance, a method of relating these two quantities must be found in order to make SSM/I data relevant to present theories of surface scatter. I have outlined how this can be done, providing we have some a priori knowledge of the wave field—the dominant wave length. This independent piece of information is not available from the SSM/I, but must be derived from another source — satellite Synthetic Aperture Radar data, in situ buoy data, or modeled predictions of wave spectra as is produced by the Global Spectral Ocean Model in operation at the Fleet Numerical Oceanography Center.

In addition to a tool for post-analysis of acoustic data, the SSM/I data is also useful as a real-time planning aid for the optimal deployment of acoustic platforms during acoustic exercises.

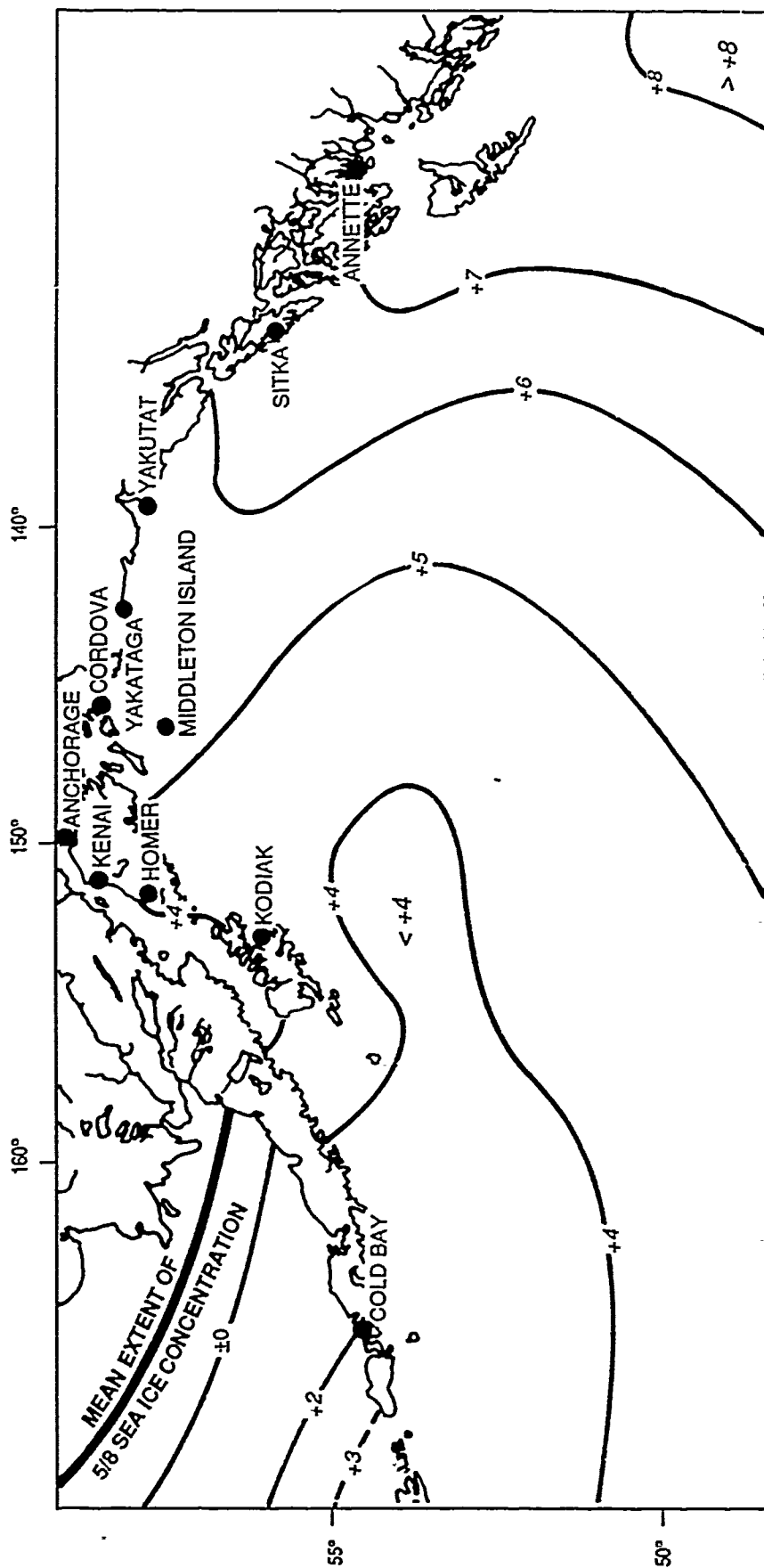


Figure 1. Contours of mean sea surface temperature (SST in °C) during the month of April in the Gulf of Alaska taken from Brower et al. (1977). The warming effect of the Alaskan Coastal Current is evident in the curvature of the mean SST near the coast.



Figure 2. NOAA-11 AVHRR image of sea surface temperature collected on 26 April, 1991. The region lies to the southeast of the Aleutian Island Chain. Note the cold eddy sitting athwart the path of the Alaskan Coastal Current and effectively blocking the flow of warm water.

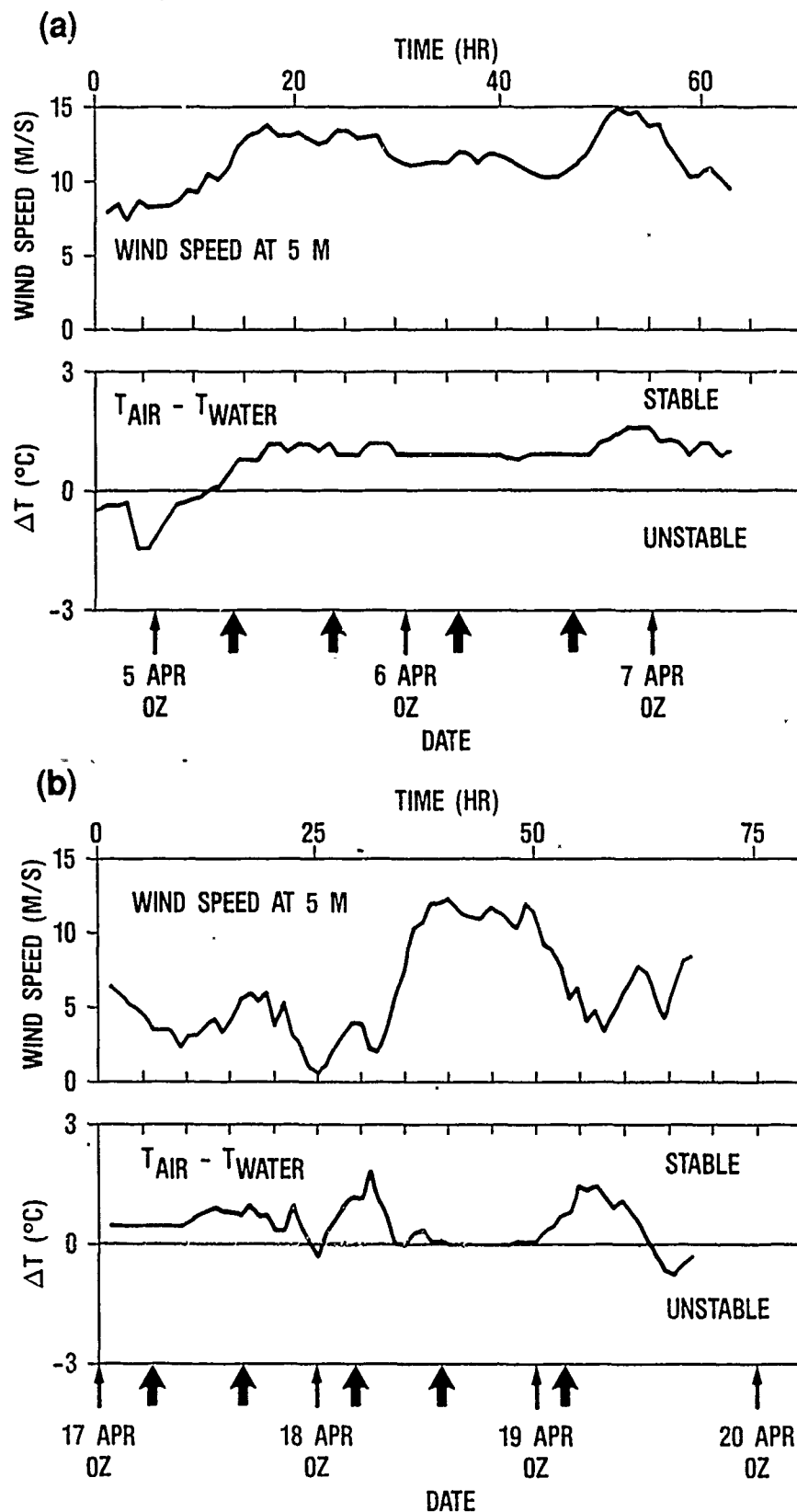


Figure 3. Wind speed and air-sea temperature difference recorded by the NOAA Data buoy #46003 located at 51.9°N 155.7°W. Solid arrows indicate times of the SSM/I overpass: (a) Wind event of 5-6 April (b) Wind event of 18-19 April.

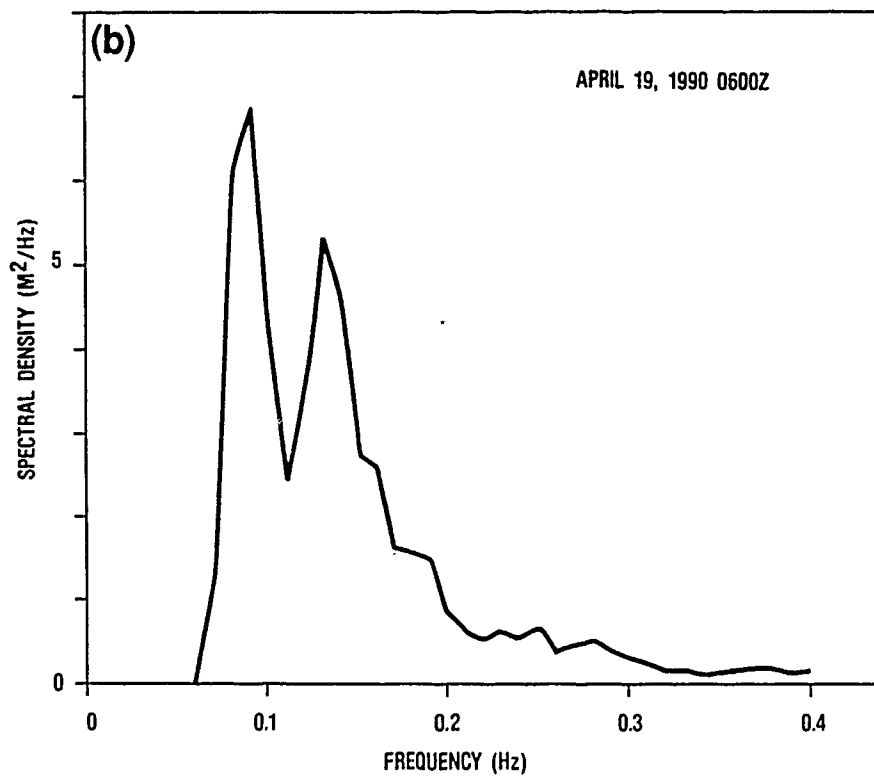
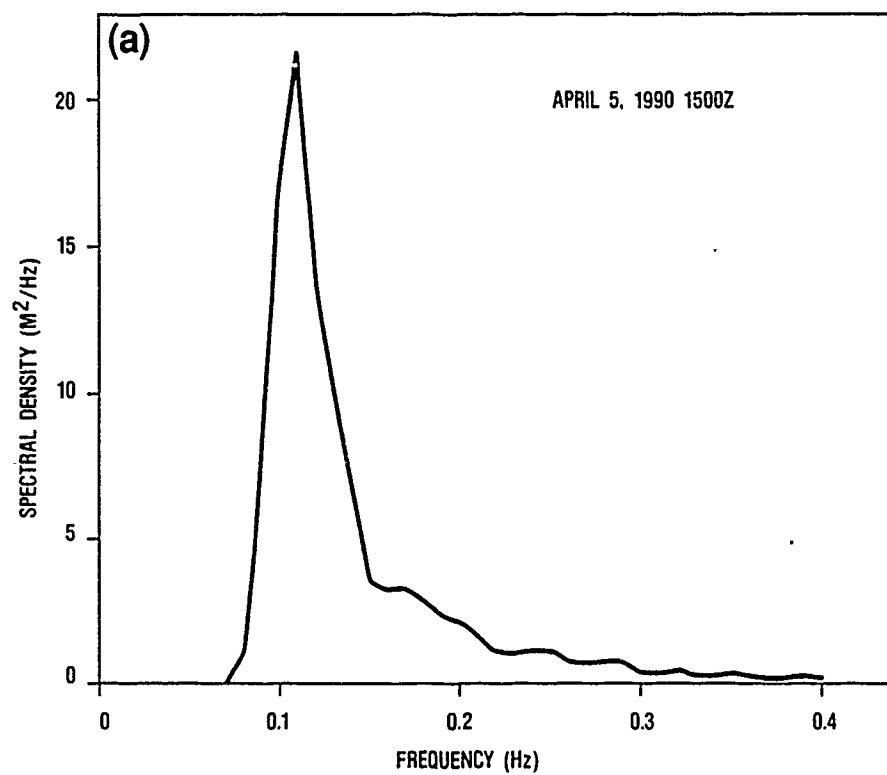


Figure 4. Elevation power spectra recorded by NOAA Data Buoy #46003 on (a) 5 April and on (b) 19 April.

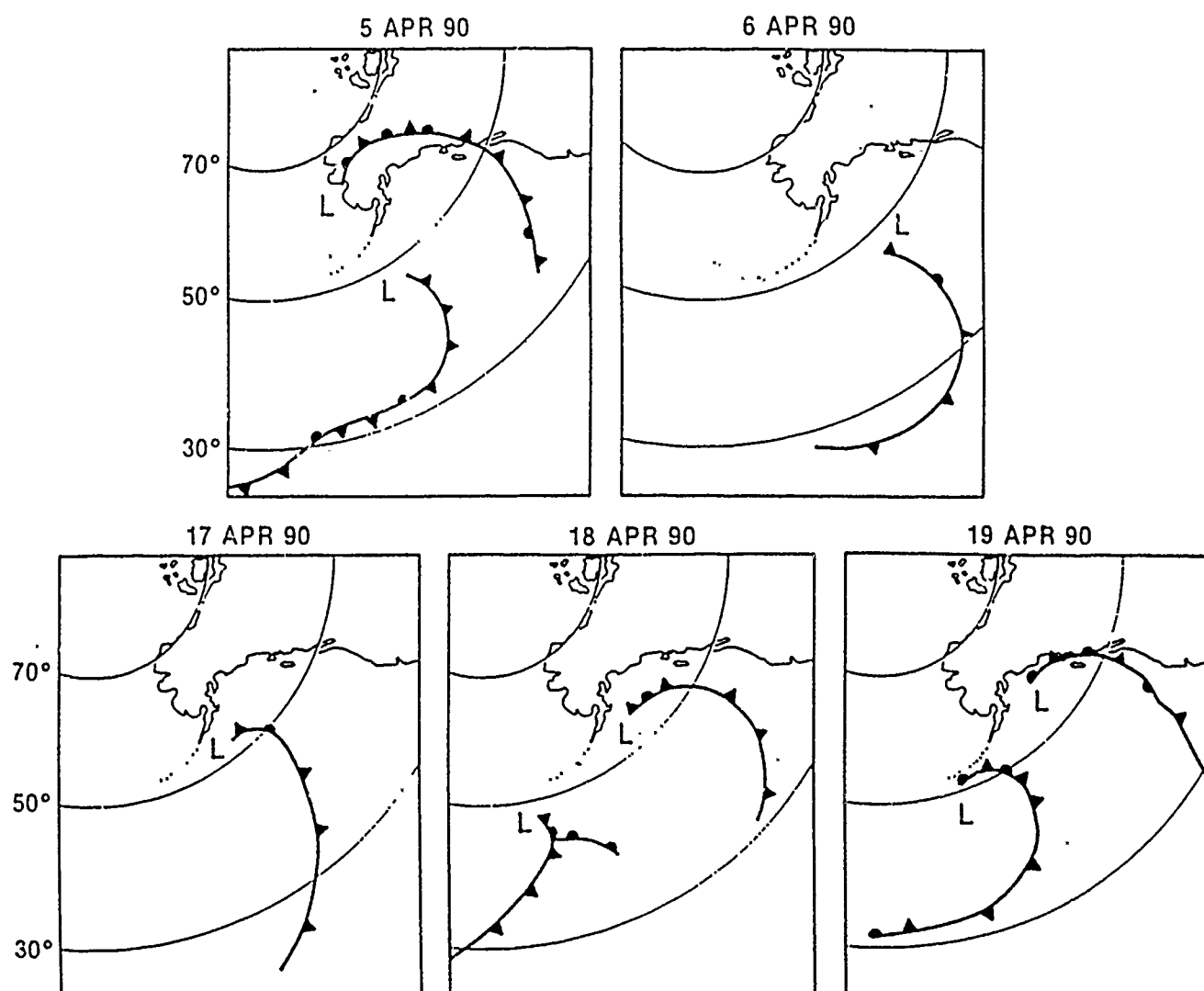
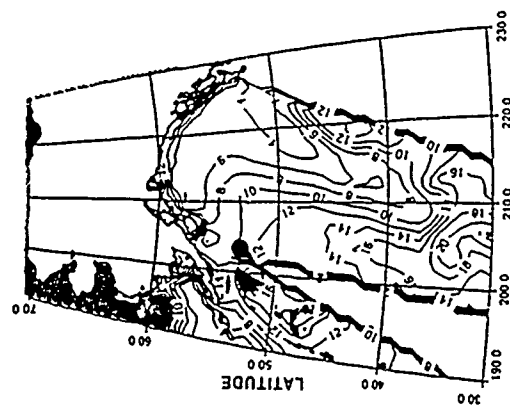
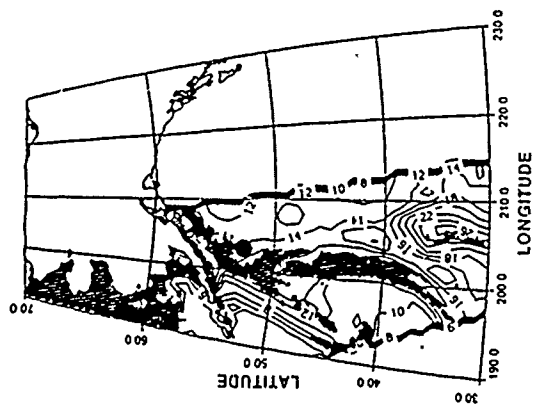


Figure 5. Frontal analysis derived from National Weather Service surface pressure analysis for 5-6 April and for 17-19 April. Low pressure systems move into the Gulf of Alaska from the southwest. Wind event of 5-6 April is associated with the arrival of a low pressure system. Event of 18 April is associated with steepening of pressure gradients between two "lows."

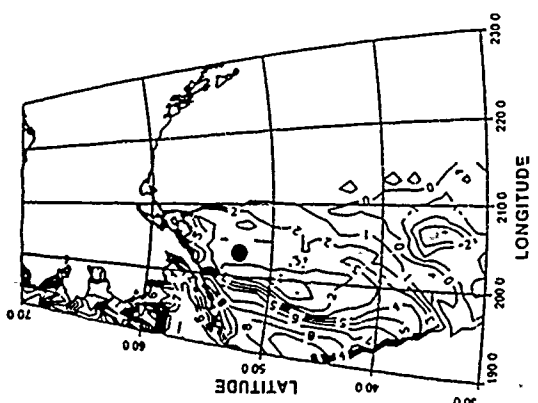
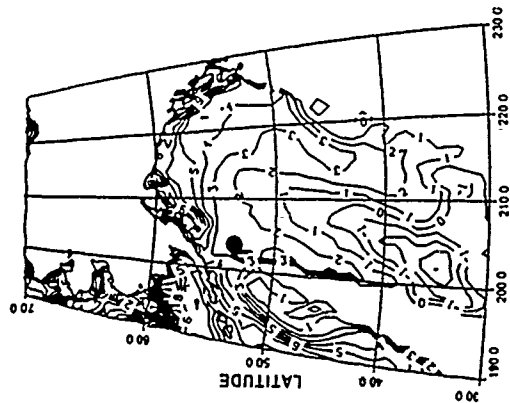
Figures 6-7. SSM/I - derived RMS wave slope, sea foam coverage, and water vapor under the satellite track. Heavy black dot indicates the location of NOAA Data Buoy #46003. Areas of precipitation are denoted by blackened regions on water vapor contours. Note steep waves and heavy whitecapping on 5 April at 1621Z behind front extending southward from data buoy.



April 5, 1990
0440Z



April 5, 1990
1621Z

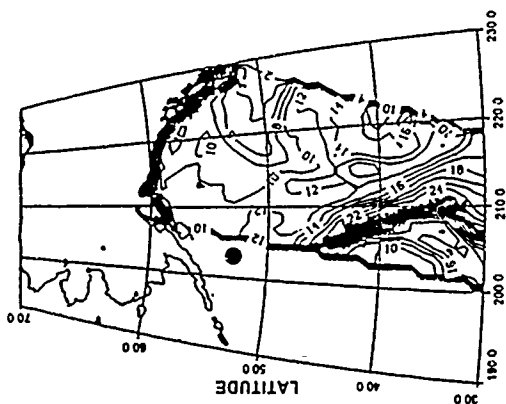


WATER VAPOR (KG/M²)

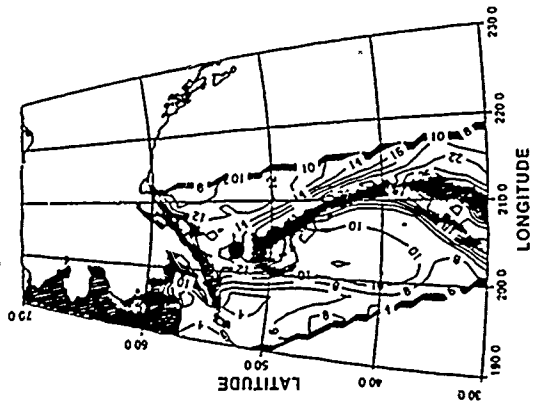
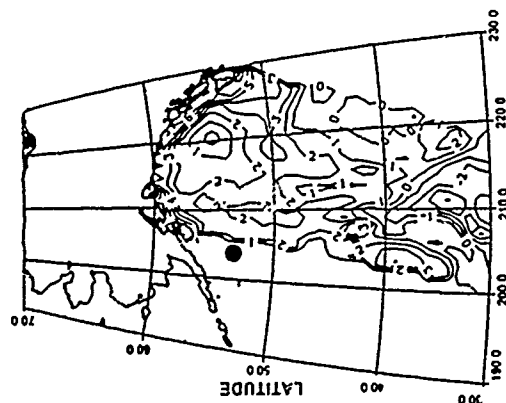
SEA FOAM COVERAGE (%)

RMS WAVE SLOPE (M/S)

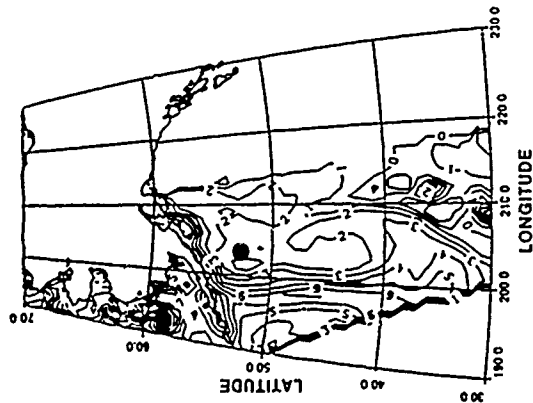
Figure 6.



April 6, 1990
0437Z



April 6, 1990
1608Z



WATER VAPOR (KG/M²)

SEA FOAM COVERAGE (%)

RMS WAVE SLOPE (M/S)

Figure 7.

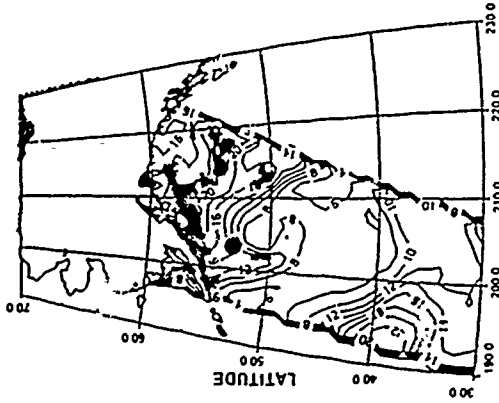
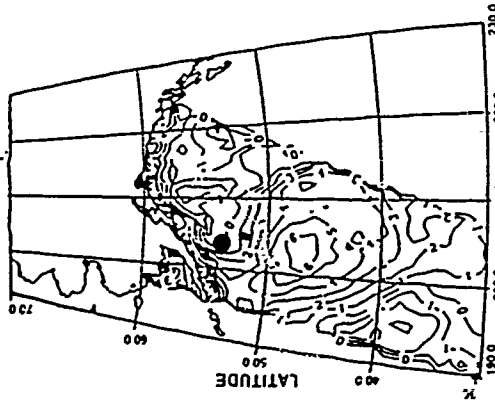
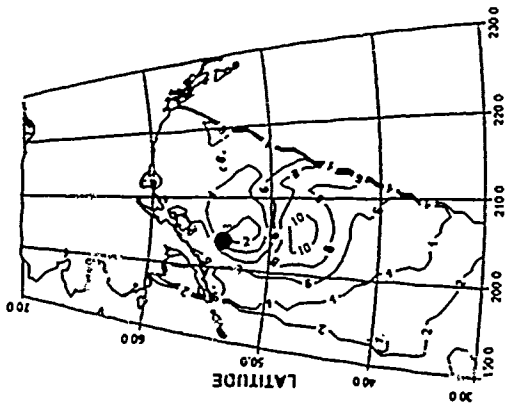
Figures 8-10. SSM/I-derived RMS wave slope, sea foam coverage, and water vapor under the satellite track for 17-19 April. Steep waves and heavy whitecapping occur 800 km directly south of the buoy on 18 April. Negative values for sea foam indicate that retrieval algorithm was not able to overcome the effect of high water vapor concentration.

SEA FOAM COVERAGE (%)

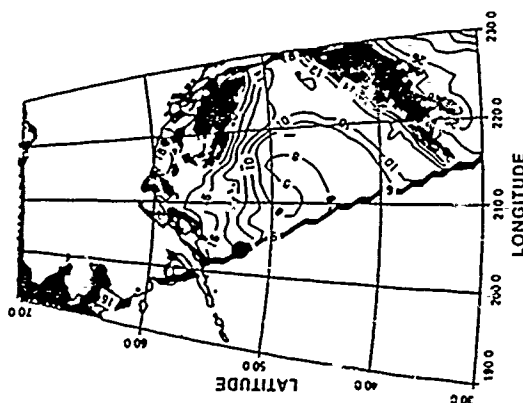
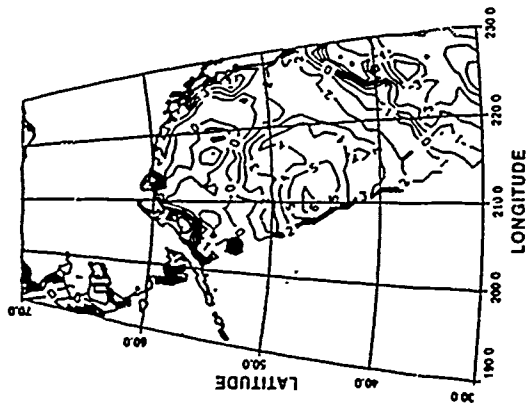
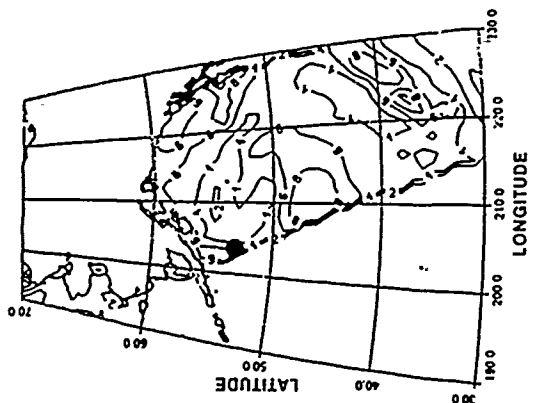
RMS WAVE SLOPE (M/S)

Figure 8.

April 18, 1990
0520Z



April 18, 1990
1510Z



RMS WAVE SLOPE (M/S)

SEA FOAM COVERAGE (%)

WATER VAPOR (KG/M²)

Figure 9.

The figure consists of three maps of the North Atlantic region, each showing a different meteorological variable. The maps are arranged horizontally, with the same geographic area (Latitude 30°N to 70°N, Longitude 190°W to 230°W) shown in each. The maps are labeled as follows:

- RMS WAVE SLOPE (M/S):** The leftmost map shows contours of root-mean-square wave slope. Contour values range from 0.1 to 2.0 m/s, with higher values generally found in the central and eastern parts of the basin.
- S&A FOAM COVERAGE (%):** The middle map shows contours of Sea and Air foam coverage. Contour values range from 0 to 10%, with higher coverage typically observed in the central and eastern North Atlantic.
- WATER VAPOR (KG/M²):** The rightmost map shows contours of water vapor. Contour values range from 5 to 25 kg/m², with higher values concentrated in the central and eastern North Atlantic.

Each map includes a coordinate grid with latitude lines at 30.0, 40.0, 50.0, 60.0, and 70.0 degrees North, and longitude lines at 190.0, 200.0, 210.0, 220.0, and 230.0 degrees West. The contour lines are labeled with their respective numerical values.

SLA FOAM COVERAGE (%)

WATER VAPOR (KG/M²)

Figure 10.

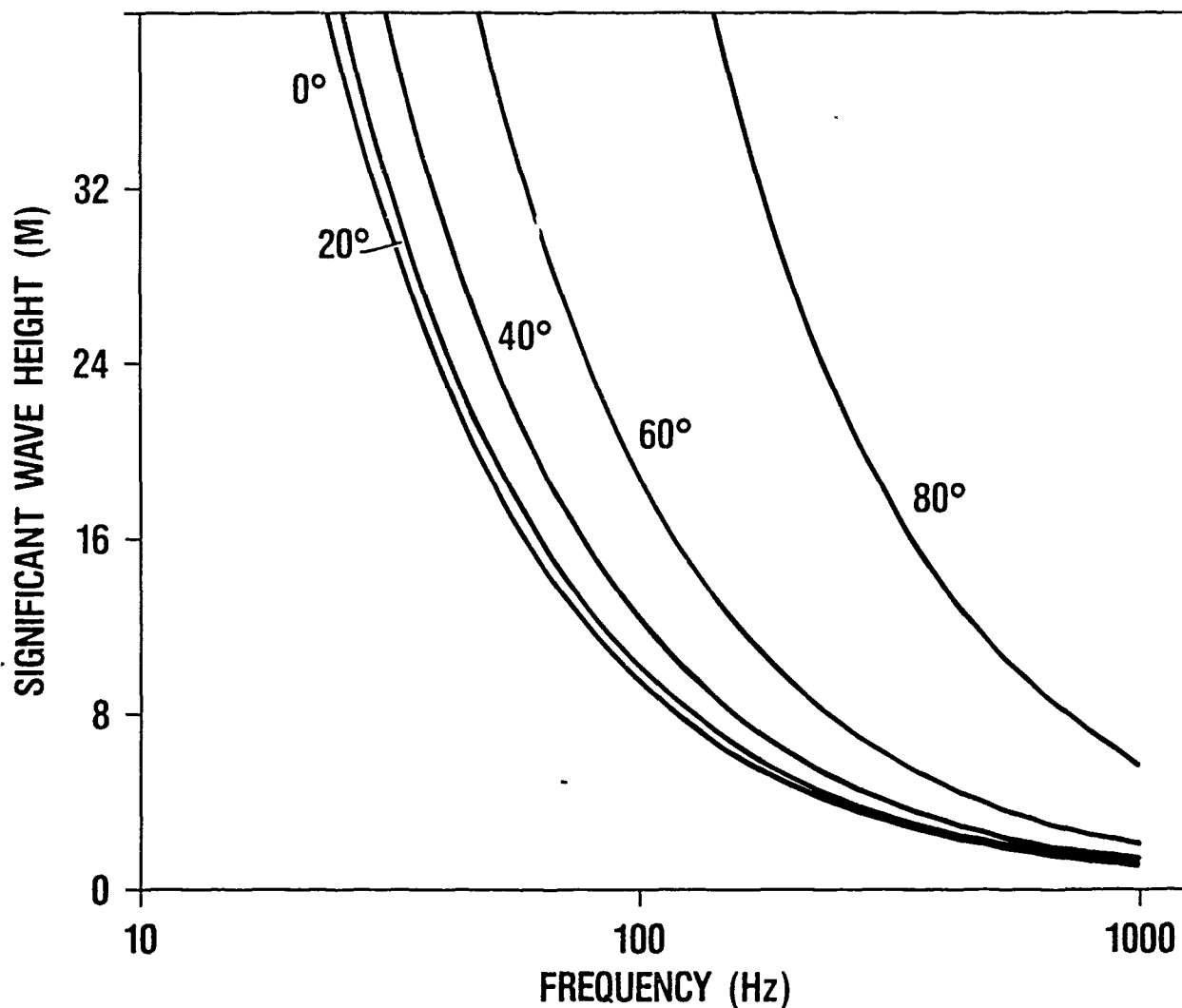


Figure 11. Kirchoff "large amplitude" acoustic wave approximation is valid in region to the right of the relevant curve. Each curve is parameterized by the incident angle at which the acoustic wave impinges on the sea surface. The X axis is acoustic frequency. Under most realistic sea conditions this approximation holds for incident angles less than 60° and for frequencies greater than 1 KHz.

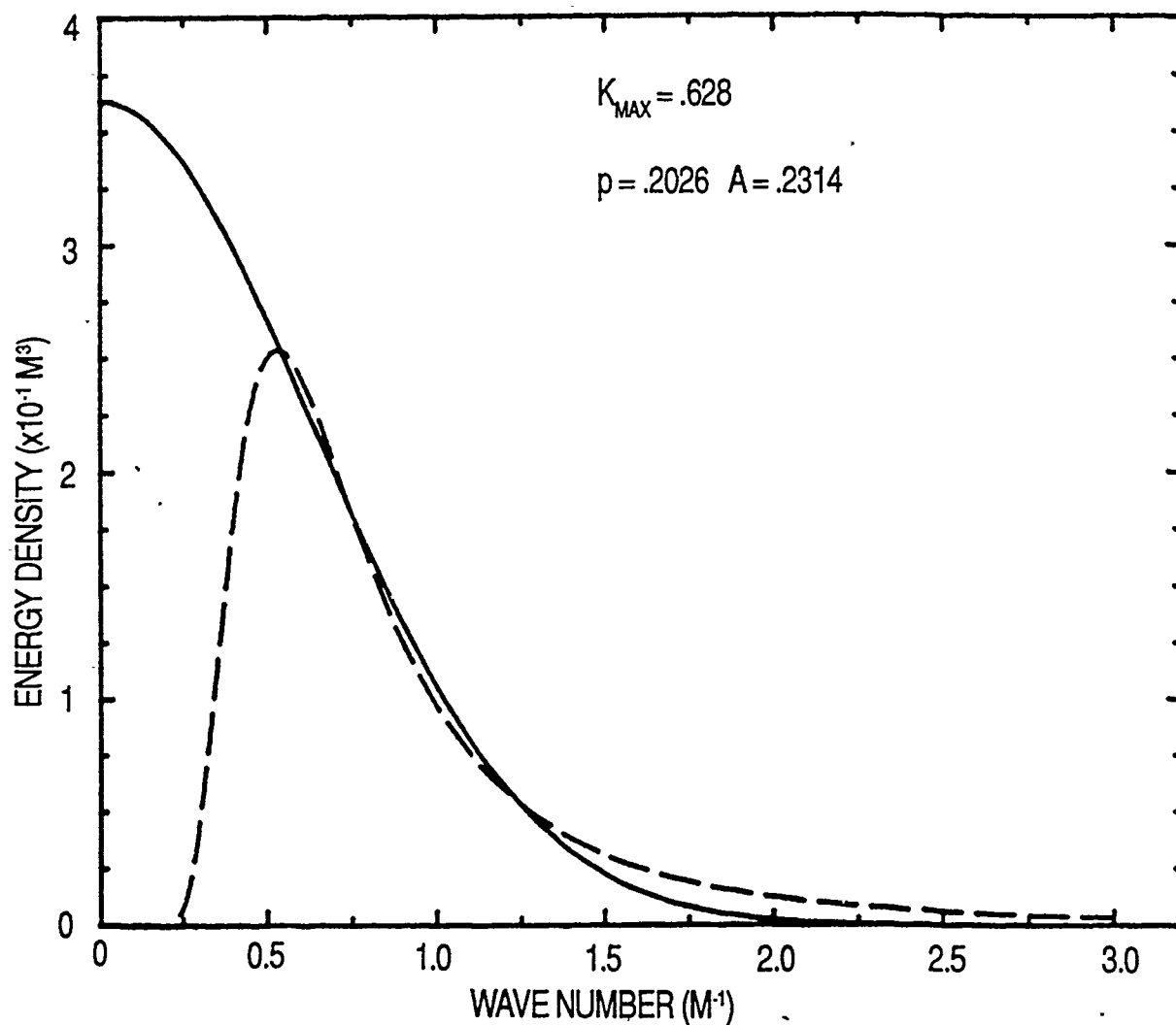


Figure 12. A Pierson-Moskowitz spectrum for a 10 m dominant wavelength superimposed on the best-fit Gaussian function. The least-squares fit is performed only for wavelengths greater than the dominant wave i.e., for the "equilibrium" range.

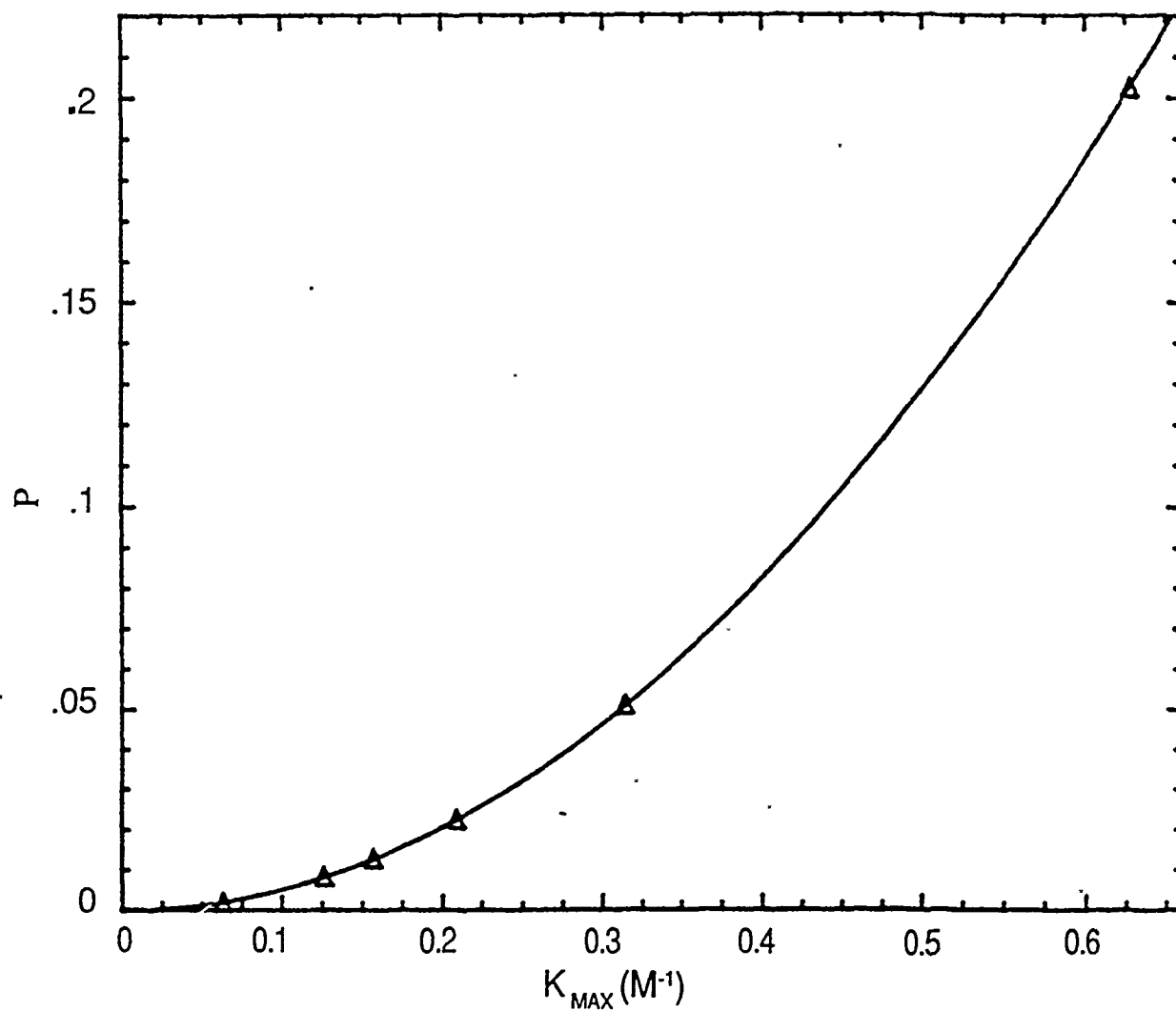
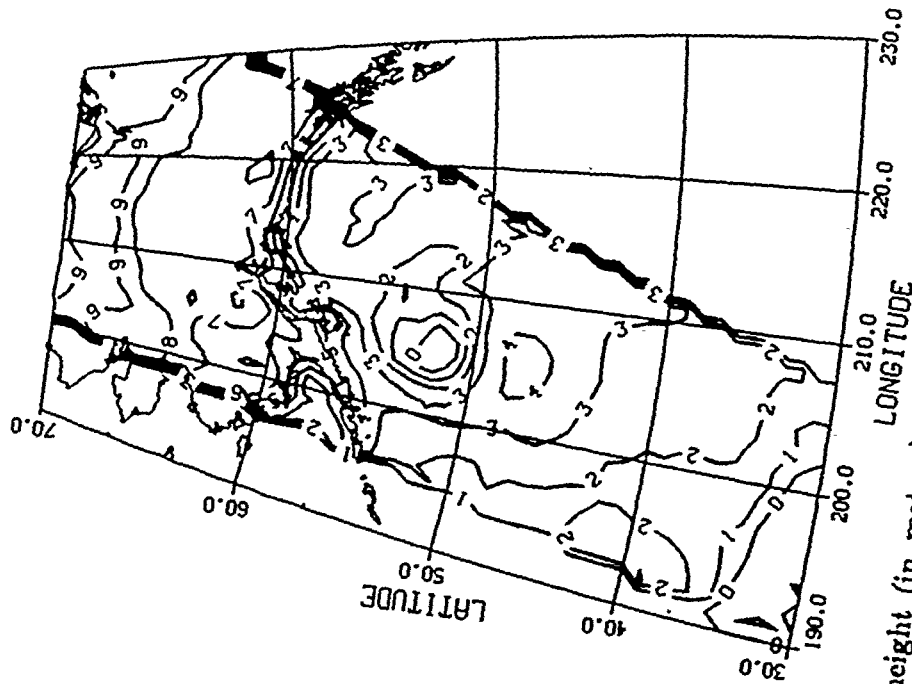
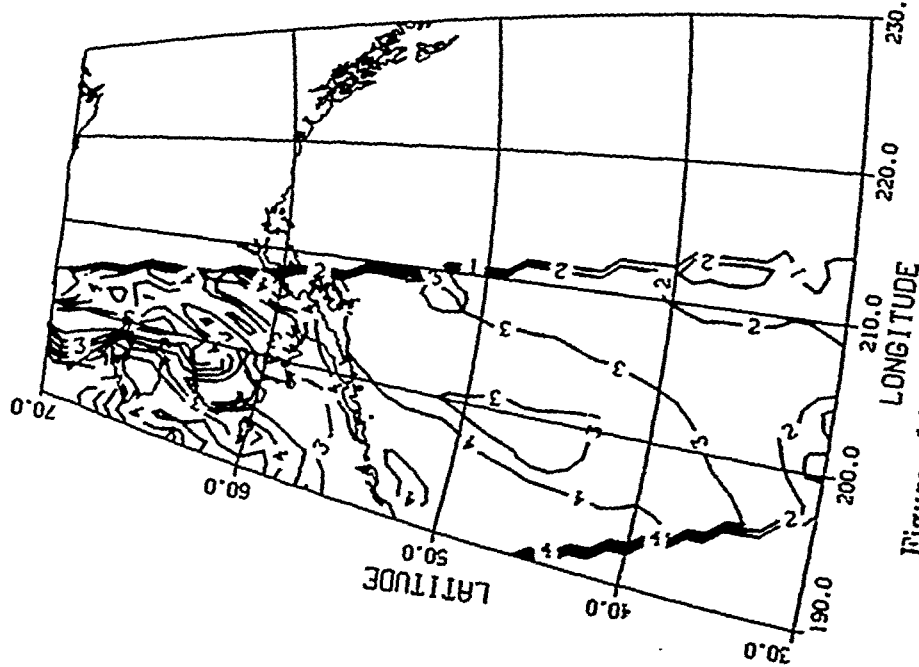


Figure 13. The Gaussian parameter p , plotted against the Pierson-Moskowitz spectral parameter, k_{maz} , for dominant wavelengths between 10 m and 100 m.



Figures 14-15. Maps of significant wave height (in meters) for 5 April and 18 April, respectively, resulting from the application of equation 9 to RMS wave slope data of the same date. The dominant wavelength was obtained from the wave spectra that were derived from the buoy data (figure 4).

REFERENCES

- Brower, W.A., H.F. Diaz, A.S. Prechtel, H.W. Searby, and J.L. Wise (1977). Climatic Atlas of the Outer Continental Shelf Waters and Coastal Regions of Alaska Volume I Gulf of Alaska. Arctic Environmental Information and Data Center, University of Alaska, 439 pp.
- Cox, C.S. and W.H. Munk (1954). Measurements of the Roughness of the Sea Surface from Photographs of Sun Glitter. *J. of Am. Optical Society* 44:838-850.
- Smith, P.M. (1991). On the Introduction of Special Sensor Microwave Imager (SSM/I) Data into the ANDES Acoustic Ambient Noise Model. Naval Oceanographic and Atmospheric Research Laboratory, SSC, MS, NOARL Technical Note 120.
- Thorsos, E. (1988). The validity of the Kirchhoff approximation for rough surface scattering using a Gaussian roughness spectrum. *J. Acoust. Soc. Am.*, 83, 78 pp.
- Ulaby, F., R. Moore, and A. Fung (1982). Microwave Remote Sensing Active and Passive. Volume II, Addison-Wesley, 1064 pp.

DISTRIBUTION

Space and Naval Warfare Systems Command
2511 Jeff Davis Highway
Washington, D.C. 2033-5100
ATTN: LCDR William Cook

Naval Oceanographic and Atmospheric Research Laboratory
Stennis Space Center, MS 39529
ATTN: Code 300
Code 330
Code 320
Code 321
Code 222 (Mr. Paul Bucca)
Code 243 (Dr. Richard Love)
Code 221 (Mr. Richard Keiffer)
Code 245 (Dr. Joel Newcomb)
Code 245 (Mr. Hassan Ali)
Code 125L (6)
Code 125P

Johns Hopkins Applied Physics Laboratory
Johns Hopkins Road
Laurel, MD 20723-6099
ATTN: Mr. Jeffrey Hanson
Mr. Scott Hyek

U.S. Naval Observatory
34th & Massachusetts Ave., NW
Washington, D.C. 20392-1800
ATTN: Mr. Donald Montgomery

Scientific Applications International Corporation
1710 Goodridge Drive
McLean, VA 22102
ATTN: Mr. William Renner